SUPPLEMENTARY INFORMATION

Mapping the mechanical stiffness of live cells with the scanning ion conductance microscope

Johannes Rheinlaender and Tilman E. Schäffer

Figure S1: Relation between slope and stiffness

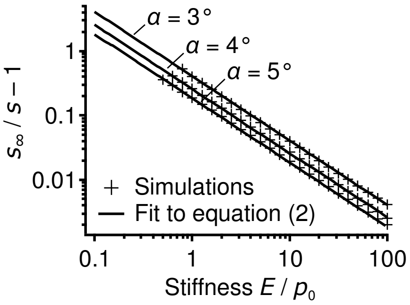

Figure S1. Relation between the slope of the calculated IZ-curves between 98% and 99% current, s, and the sample stiffness, E, obtained from finite element calculations. Different values of pipette half cone angle α and a constant pipette wall thickness $r_i/2$ were used. Plotting $\left(s_\infty/s-1\right)$ vs. E/p_0 on a double-logarithmic scale shows the calculated data points on lines with a gradient of -1 over several orders of magnitude. This leads to the functional relation expressed by equation (2). The geometrical parameter A was determined by fitting equation (2) and is tabulated in Supplementary Table 1.

Figure S2: Statistical variation of the measured slope in IZ-curves

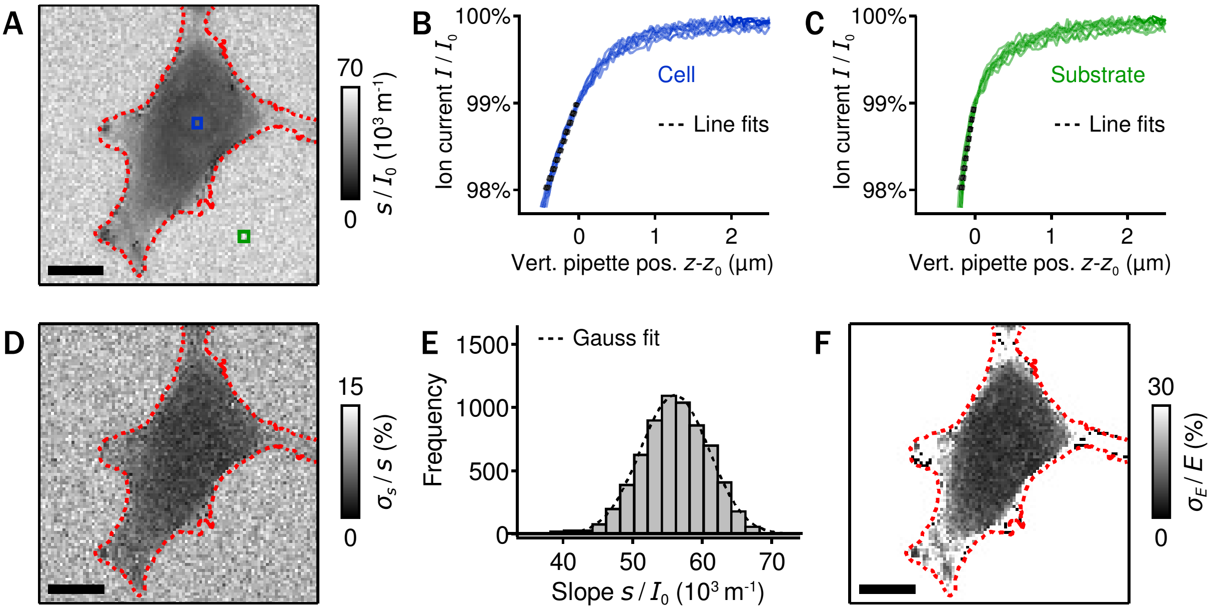

Figure S2. Analysis of the statistical variation of the measured slope in IZ-curves. The measurement of the ion current is influenced by electronic noise, which is mainly Johnson noise of the electrical resistance of the nanopipette[1]. The noise of the ion current can therefore be estimated as $\sigma_I = \sqrt{4\,k_\mathrm{B} T\,\Delta f / R} \cong 4\,\mathrm{pA}$, where k_B is the Boltzmann constant, $\Delta f = 10\,\mathrm{kHz}$ is the bandwidth of the ion current measurement and $R = V_0 / I_0 \cong 10\,\mathrm{M\Omega}$ is the typical electrical resistance of the pipettes used here. Due to this noise the measured slope of an IZ-curve is also subject to a statistical variation. (A) Measured slope s (normalized with respect to the maximum ion current in the IZ-curve, $I_0 = 9.3\,\mathrm{nA}$) of the IZ-curves on the living fibroblast shown in Fig. 1C (the cell's outline is indicated by the dashed red contour line). (B,C) Set of nine IZ-curves in a small region each (B) on the cell and (C) on the substrate (regions indicated by colored boxes in A) to illustrate the reliability of the method. It can be seen that the IZ-curves are reproducible and vary just within the statistical ion current noise. The measured relative slope of the shown IZ-curves is $s / I_0 = (24.8 \pm 1.4) \cdot 10^3\mathrm{m}^{-1}$ and $(56.1 \pm 6.5) \cdot 10^3\mathrm{m}^{-1}$ (average ± standard deviation) for the cell and the substrate, respectively. These standard deviations correspond well with the estimates from the linear regression ($1.1 \cdot 10^3\mathrm{m}^{-1}$ and $6.1 \cdot 10^3\mathrm{m}^{-1}$, respectively). (D) Estimate of the relative standard deviation of the slope σ_s from the linear regression of the IZ-curves. The relative standard deviation of the slope is lower on the cell (about 4%) and larger on the substrate (about 10%). This difference is due to the fact that the ion current drops more rapidly on stiffer regions of the sample and thus fewer data points contribute to the linear regression. Since the slope for infinite stiffness, s_∞, is used for the quantification of the local sample stiffness [equation (1)] a more robust value for s_∞ was determined by averaging the slope of many IZ-curves on the substrate. (E) Histogram of the slope of the IZ-curves on the substrate. It can be seen that the variation of the slope on the substrate is well described by a Gaussian distribution. Its standard deviation $\sigma_s / I_0 = 5 \cdot 10^3\ \mathrm{m}^{-1}$ (9% of the average) is in well agreement both with the standard deviation of the IZ-curves in C and with the estimate for the standard deviation from the linear regression of the single IZ-curves shown in D. The variation of the measured slope is therefore predominantly statistical. Hence, the slope for infinite stiffness can be estimated well by the average slope on the substrate $s_\infty = (4.778 \pm 0.005) \cdot 10^4\ \mathrm{m}^{-1}$ (mean ± standard error of the mean). Due the noise of the measured slope also the resulting stiffness for an IZ-curve is subject to noise. (F) Relative error of the measured stiffness σ_E / E on the cell, which is estimated with $\sigma_E / E \approx \sigma_s / E \cdot \mathrm{d}E / \mathrm{d}s = \sigma_s / s \cdot \left(1 - s / s_\infty\right)^{-1}$ based on equation (1); the values on the substrate were omitted. The relative error of the stiffness is on the order of 3–10% on the soft regions but can be significantly larger on the stiff regions. Scale bars: 15 µm.

Figure S3: Test for mechanical contact

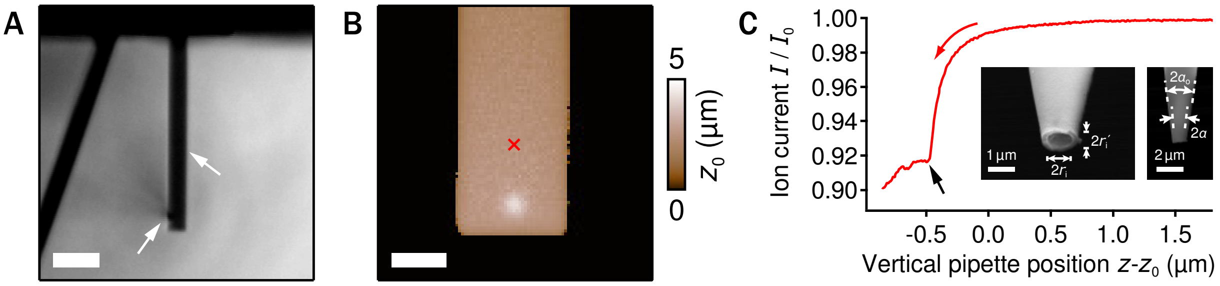

Figure S3. Test for mechanical contact by recording an IZ-curve on an AFM cantilever for a typical nanopipette used in this study. (A) Optical image of the pipette (left arrow) in proximity to an AFM cantilever (right arrow) (MLCT B-lever, Bruker AFM Probes) mounted on the bottom of a petri dish with the cantilever tip pointing upwards. (B) SICM topography image of the tip region of the cantilever. (C) IZ-curve on the cantilever (location indicated by cross in B) with zero applied pressure. The event of mechanical contact between the pipette tip and the cantilever can be identified by the kink in the IZ-curve (here at 92% ion current, straight arrow). At this position the cantilever started to deflect and the ion current thus did not decrease any further at first. This proves that for 98% current this pipette was not in mechanical contact with the sample. The inset shows scanning electron microscopy images of the tip region of the pipette used here, taken at angles of 45° (left image) and 90° (right image) relative to the pipette axis. The pipette opening was almost perfectly circular since the ratio of the inner opening radius $r_i = 450 \pm 20$ nm to the projected inner opening radius $r_i' = 310 \pm 20$ nm is approximately $\sqrt{2}$ (which is expected for a viewing angle of 45°). The inner half cone angle was found to be typically $\alpha = 4°$ for the pipettes used here (estimated from the outer half cone angle $\alpha_o \cong \alpha \cdot r_o / r_i$). Scale bars: 50 µm (A) and 10 µm (B).

Figure S4: Influence of cytochalasin D on cell stiffness

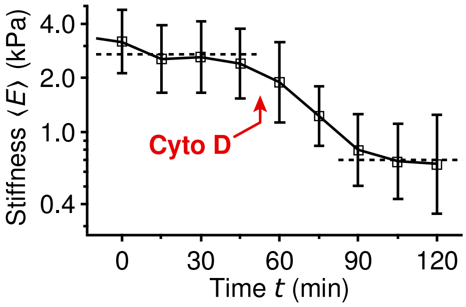

Figure S4. Influence of cytochalasin D on the average stiffness of the fibroblast cell shown in Fig. 3. After the addition of 2 µM cytochalasin D (arrow) the log-average stiffness ⟨*E*⟩ decreased within 30 min from 2.7 ± 0.3 kPa to 0.7 ± 0.1 kPa (factor of 3.9). A similar factor has also been observed in AFM experiments[2].

Figure S5: Evaluation of the lateral resolution

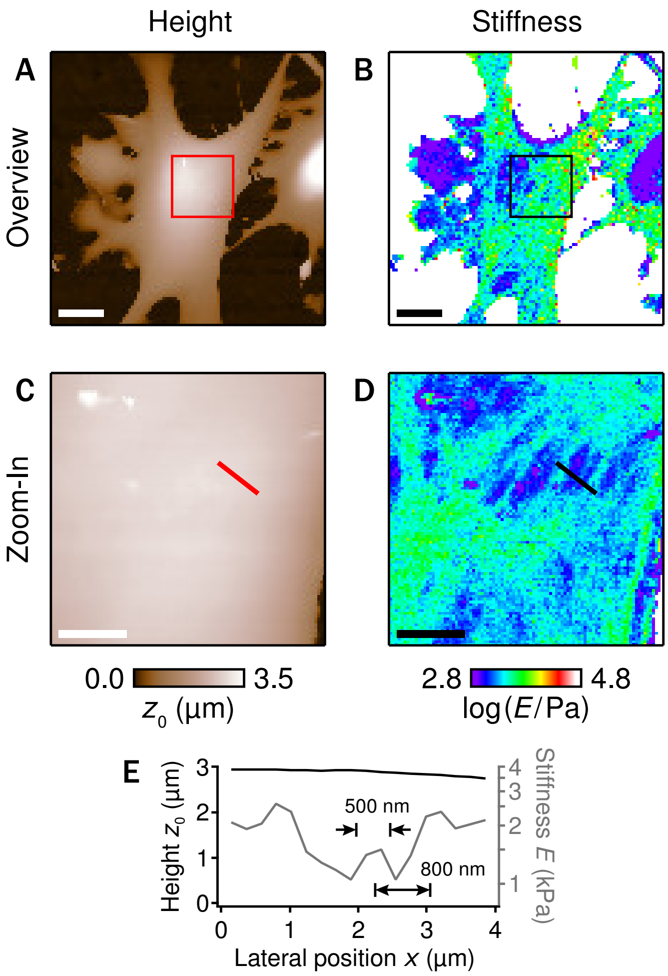

Figure S5. Evaluation of the lateral resolution in stiffness maps. To show that our method can achieve sub-micrometer lateral resolution a high-resolution stiffness map was recorded on a living cell using a pipette with an opening radius of $r_i \approx 100$ nm. (A) Overview topography image and (B) stiffness map. (C) Zoom-in topography image and (D) stiffness map recorded in the region marked by boxes in *A* and *B*. While the topography appears relatively smooth, the stiffness varies between 1 and 10 kPa and substructures of the cytoskeleton can be seen. (E) Cross section of height and stiffness across three cytoskeleton fibers (location indicated by lines in C and D). The full width at half maximum of the fiber in the middle is 500 nm; the peak-to-peak distance between the two fibers on the right is 800 nm. Since the fibers are clearly resolved in the stiffness map (D), we estimate a lateral resolution of 500–800 nm, which corresponds to 5–8r_i. Scale bars: 15 μm (A, B) and 5 μm (C, D).

Figure S6: SICM stiffness mapping with different pipette opening diameters

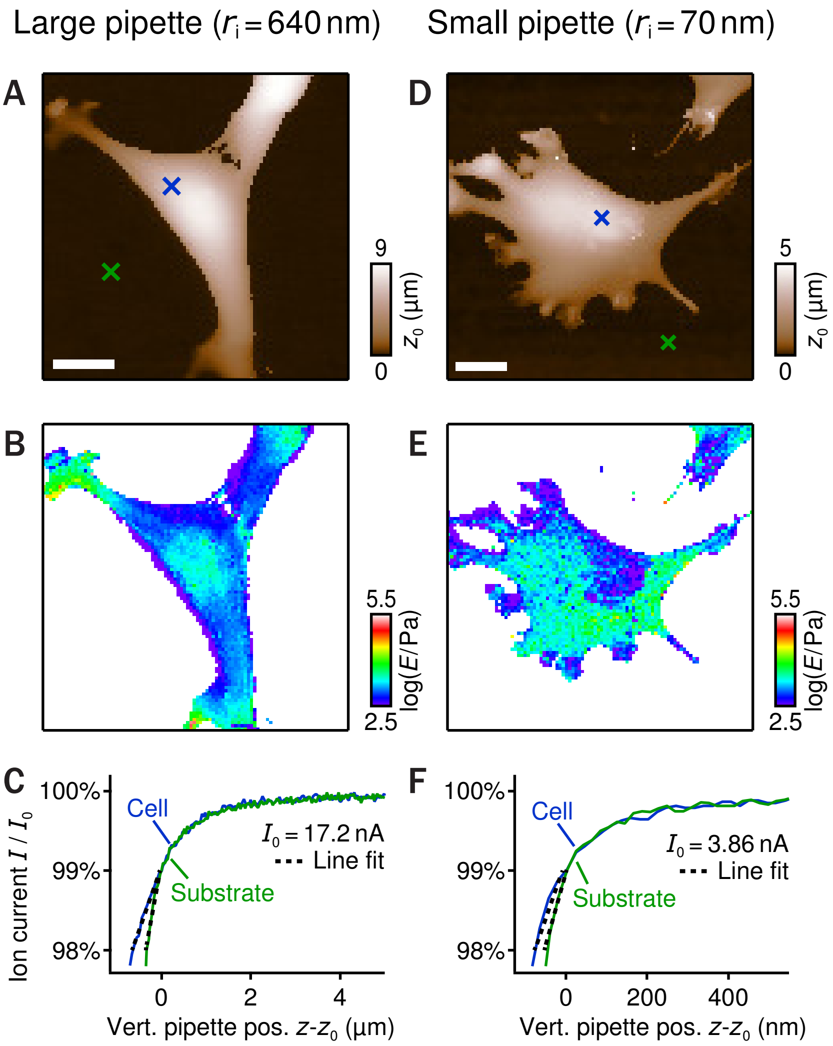

Figure S6. SICM stiffness mapping with different pipette sizes. Stiffness maps of living cells were recorded with a large pipette ($r_i = 640$ nm, left column) and with a small pipette ($r_i = 70$ nm, right column). (A) Topography image, (B) stiffness map, and (C) IZ-curves on the substrate and on the cell recorded with the large pipette ($V_0 = 100$ mV, positions indicated by crosses in A). (D) Topography image, (E) stiffness map, and (F) IZ-curves on the substrate and on the cell recorded with the small pipette ($V_0 = 200$ mV, positions indicated by crosses in D). The following aspects can be seen by comparing the IZ-curves: First, the ion current drop occurs within a larger vertical distance for the large pipette. Second, the functional form of the IZ-curves is independent of the pipette size (the IZ-curves contain different numbers of data points since they were recorded with a similar vertical approach speed and sample rate).

Figure S7: Verification of the numerical model

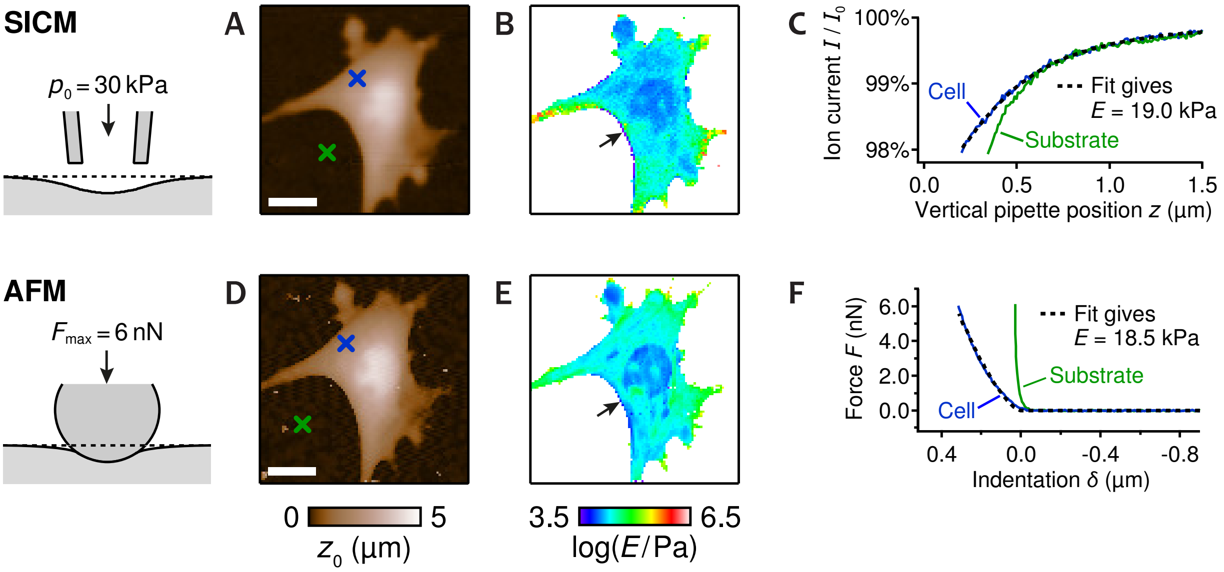

Figure S7. Verification of the numerical model by directly comparing experimentally observed and calculated IZ-curves (ion current vs. vertical pipette position). (A) SICM topography image and (B) stiffness map of a fixed fibroblast, recorded with an applied pressure of $p_0 = 30$ kPa. (C) IZ-curves on the cell and on the substrate (positions indicated by crosses in A). The IZ-curve on the substrate was fitted with calculated IZ-curves for infinite sample stiffness and a pipette inner half cone angle of $\alpha = 4°$. The only fit coefficient was the pipette opening radius, giving $r_i = 450$ nm. This value is in agreement with the radius estimated from the maximum ion current[3] [$r_i = I_0/(\pi\sigma V_0 \tan\alpha) = 410\,\text{nm}$ using $I_0 = 12$ nA, $V_0 = 100$ mV, $\sigma = 1.35$ S m^{-1} for PBS at room temperature]. The IZ-curve on the cell was fitted with FEM data for finite stiffness while holding α and r_i constant and resulted in a stiffness of $E = 0.63p_0 = 19.0$ kPa. The numerical IZ-curves (fits) closely match the experimental data indicating that the finite element model describes the qualitative behavior of the ion current well. To verify the model also quantitatively, an AFM force map was recorded on the same cell afterwards: (D) AFM topography image (at the point of contact) and (E) stiffness map. An AFM cantilever with a spherical tip of radius 0.94 µm, a spring constant of 0.226 N m^{-1} (determined by the thermal noise calibration method[4]) and a maximum applied force of 6 nN was used to approximately match shape and depth of the SICM and AFM indentation profiles (shown to scale in the schematics on the left in the figure). (F) Force vs. indentation curve at the same positions on the cell (positions indicated by crosses in D). Fitting the Hertz model for a spherical indenter gave a sample stiffness of $E = 18.5$ kPa (assuming a Poisson's ratio of $v = 0.5$). From the stiffness maps (B and E) it can be seen that a close agreement between SICM and AFM stiffness results was found. The log-average stiffness (Young's modulus) of the cell was measured as $\langle E \rangle = 18.6$ kPa by the SICM and as 18.9 kPa by the AFM. Hence, the numerical model also quantitatively well describes the deformation of the sample and the resulting ion current. As known from AFM, indentation measurements on sample regions where the surface is strongly inclined or curved might be affected by artifacts. This occurs, for example, on the edges of the cell (arrows in B and E) where the cell appears relatively soft both in the SICM and the AFM stiffness map. Scale bars: 15 µm.

Table S1: Influence of the pipette geometry on *A*

Geometrical parameter *A* for different values of inner half cone angle α and wall thickness of the pipette.

inner half cone angle α	3°			4°			5°		
wall thickness (in units of r_i)	0.25	0.5	1.0	0.25	0.5	1.0	0.25	0.5	1.0
geometrical parameter *A*	0.46	0.40	0.33	0.29	0.26	0.21	0.21	0.18	0.15

Supplementary Note: Fluid flow in a conical pipette

The maximum volumetric flow rate through the pipette is[6]

$$Q_0 = \frac{3\pi \tan\alpha}{8\eta} r_\mathrm{i}^3 p_0 \tag{S1}$$

where η is the viscosity of the fluid ($\eta = 0.7$ mPa s for water at 37°C). The fluid velocity is maximum in the center of the pipette opening. Since the flow profile is parabolic (Hagen-Poiseuille-like) the maximum fluid velocity is twice the average fluid velocity in the pipette opening:

$$v_\mathrm{max} = 2v_\mathrm{avg} = 2\frac{Q}{\pi r_\mathrm{i}^2} = \frac{3\tan\alpha}{4\eta} r_\mathrm{i} p_0 \,. \tag{S2}$$

For the pipettes and the applied pressures used here a typical fluid velocity is $v_\mathrm{max} \approx 10\ \mathrm{cm\ s^{-1}}$. An upper limit of the Reynolds number, *Re*, can be estimated as

$$Re \approx \frac{\rho\, v_\mathrm{max} r_\mathrm{i}}{\eta} = \frac{3\tan\alpha}{4} \frac{\rho}{\eta^2} r_\mathrm{i}^2 p_0 \approx 0.01 \tag{S3}$$

where ρ is the density of the fluid ($\rho = 10^3\ \mathrm{kg\ m^{-3}}$ for water). This is far below the critical Reynolds number, Re_crit, for turbulent flow in a cone[7]

$$Re_\mathrm{crit} = \frac{12}{\tan\alpha} \approx 200 \tag{S4}$$

using a half cone angle of $\alpha = 4°$. The fluid dynamics are therefore dominated by viscous flow. However, for opening radii larger than about 10 µm turbulent flow might set in. The hydrodynamic timescale of the flow can be estimated as

$$\tau \approx \frac{r_\mathrm{i}}{v_\mathrm{max}} = \frac{4\eta}{3p_0 \tan\alpha} \approx 1\,\mu\mathrm{s}\,. \tag{S5}$$

Movie S1: Time-lapse imaging of a live NIH3T3 fibroblast cell

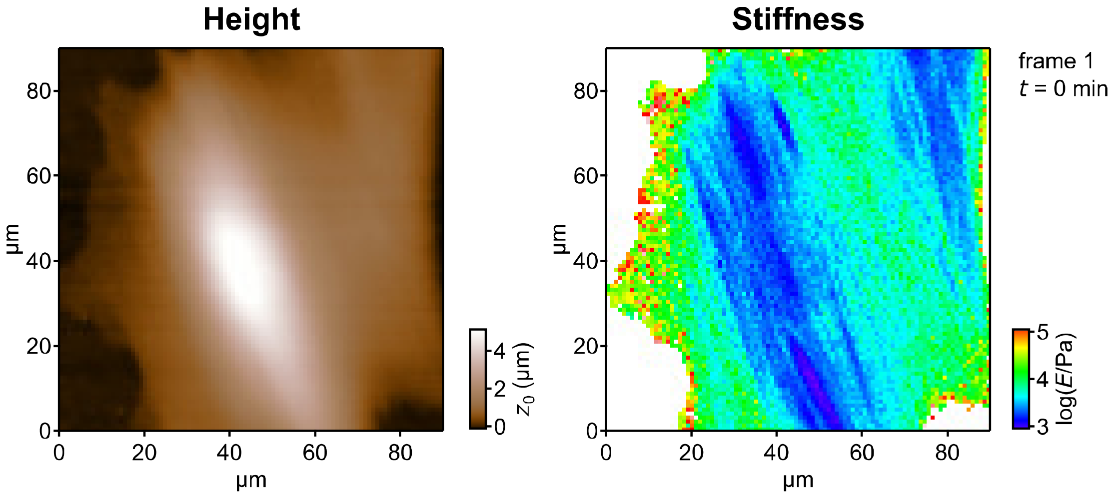

Movie S1. Time-lapse imaging of a live NIH3T3 fibroblast cell with addition of cytochalasin D. Eleven consecutive frames of height (left) and stiffness (right) images are shown (including those in Fig. 3). Acquisition time: 15 min per frame (up-scan). The movie file is available online (see ESI).

References

1. B. Sakmann and E. Neher, *Single-Channel Recording*, Springer, Heidelberg, 1995.
2. C. Rotsch and M. Radmacher, *Biophys. J.*, 2000, **78**, 520-535.
3. T. K. Chowdhury, *J. Phys. E: Sci. Instrum.*, 1969, **2**, 1087-1090.
4. S. M. Cook, T. E. Schäffer, K. M. Chynoweth, M. Wigton, R. W. Simmonds and K. M. Lang, *Nanotechnology*, 2006, **17**, 2135-2145.
5. N. Gavara and R. S. Chadwick, *Nat Meth*, 2010, **7**, 650-654.
6. D. Sánchez, N. Johnson, C. Li, P. Novak, J. Rheinlaender, Y. Zhang, U. Anand, A. Praveen, J. Gorelik, G. Frolenkov, C. Benham, M. Lab, V. Ostanin, T. E. Schäffer, D. Klenerman and Y. E. Korchev, *Biophys. J.*, 2008, **95**, 3017-3027.
7. H. Blasius, *Z. Math. Phys.*, 1910, **58**, 225-233.